Nowcast model for low-energy electrons in the inner magnetosphere

N. Yu. Ganushkina[1,2], O. A. Amariutei[1], D. Welling[2], and D. Heynderickx[3]

[1]Finnish Meteorological Institute, Helsinki, Finland, [2]Department of Atmospheric, Oceanic and Space Sciences, University of Michigan, Ann Arbor, Michigan, USA, [3]DH Consultancy BVBA, Leuven, Belgium

Abstract We present the nowcast model for low-energy (< 200 keV) electrons in the inner magnetosphere, which is the version of the Inner Magnetosphere Particle Transport and Acceleration Model (IMPTAM) for electrons. Low-energy electron fluxes are very important to specify when hazardous satellite surface-charging phenomena are considered. The presented model provides the low-energy electron flux at all L shells and at all satellite orbits, when necessary. The model is driven by the real-time solar wind and interplanetary magnetic field (IMF) parameters with 1 h time shift for propagation to the Earth's magnetopause and by the real time *Dst* index. Real-time geostationary GOES 13 or GOES 15 (whenever each is available) data on electron fluxes in three energies, such as 40 keV, 75 keV, and 150 keV, are used for comparison and validation of IMPTAM running online. On average, the model provides quite reasonable agreement with the data; the basic level of the observed fluxes is reproduced. The best agreement between the modeled and the observed fluxes are found for <100 keV electrons. At the same time, not all the peaks and dropouts in the observed electron fluxes are reproduced. For 150 keV electrons, the modeled fluxes are often smaller than the observed ones by an order of magnitude. The normalized root-mean-square deviation is found to range from 0.015 to 0.0324. Though these metrics are buoyed by large standard deviations, owing to the dynamic nature of the fluxes, they demonstrate that IMPTAM, on average, predicts the observed fluxes satisfactorily. The computed binary event tables for predicting high flux values within each 1 h window reveal reasonable hit rates being 0.660–0.318 for flux thresholds of $5 \cdot 10^4$–$2 \cdot 10^5$ cm^{-2} s^{-1} sr^{-1} keV^{-1} for 40 keV electrons, 0.739–0.367 for flux thresholds of $3 \cdot 10^4$ –$1 \cdot 10^5$ cm^{-2} s^{-1} sr^{-1} keV^{-1} for 75 keV electrons, and 0.485–0.438 for flux thresholds of $3 \cdot 10^3$ –$3.5 \cdot 10^3$ cm^{-2} s^{-1} sr^{-1} keV^{-1} for 150 keV electrons but rather small Heidke Skill Scores (0.17 and below). This is the first attempt to model low-energy electrons in real time at 10 min resolution. The output of this model can serve as an input of electron seed population for real-time higher-energy radiation belt modeling.

1. Introduction

Space weather can be defined as severe disturbances of the upper atmosphere and near-space environment that can damage modern technology on the ground and in space [*Wrenn*, 1995; *Baker*, 2001; *Iucci et al.*, 2005; *National Research Council Report*, 2008]. These disruptions are driven by changes on the Sun and the interaction of the solar wind with the Earth's magnetic field.

Energetic charged particles trapped in the radiation belts are a major source of damaging space weather effects on life and society here on Earth. They directly and adversely affect space-based technological assets, and they pose a serious risk of harm to astronauts. Understanding the physical processes that enhance the radiation belts is, therefore, a timely and pressing issue. This requires an integrated approach that combines the global topological dynamics of the magnetosphere and bulk plasma properties as well as detailed trajectory simulations of the highly energetic relativistic electrons and ions.

The observed variability of electrons in the outer radiation belt is due to the competing effects of source and loss processes, both of which are driven by solar dynamics. The pulsations of the magnetopause and the magnetotail create ultralow frequency (ULF) waves in the inner magnetosphere that resonate with the drift periods of the radiation belt particles [*Elkington et al.*, 2004; *Shprits et al.*, 2005]. The plasma sheet electron and ring current ion distributions get altered into unstable forms, exciting various plasma waves (notably VLF chorus and electromagnetic ion cyclotron (EMIC) waves) that can either energize or scatter (i.e., loose) relativistic particles [*Horne and Thorne*, 1998; *Summers et al.*, 1998; *Green and Kivelson*, 2001, 2004;

Horne et al., 2005a, 2005b; *Y. Chen et al.*, 2006; *Shprits et al.*, 2006]. Furthermore, the plasmasphere separates different types of waves such as plasmaspheric hiss and possibly EMIC waves inside the plasmapause from chorus outside and these waves not only resonate with electrons in different energy ranges but they also contribute to electron loss and acceleration in different amounts as they drift around the Earth. *Reeves et al.* [2003] showed that some geomagnetic storms enhance the radiation belts while others do not. Great strides are being made with data analysis and data assimilation techniques, but, so far, the response of the magnetosphere to solar variability is still poorly understood.

The distribution of low-energy electrons (10–150 keV) is critically important for radiation belt dynamics. This seed population is further accelerated to MeV energies by various processes. All radiation belt models must have a flux defined at a low-energy boundary at all L shells. Quite often, the boundary energy is fixed to be several keV. However, the electron flux at these energies varies significantly with geomagnetic activity. Satellite measurements cannot provide continuous measurements at 10 to a few hundreds of keV at all MLT and L shells. The electron flux at these energies is largely determined by convective and inductive electric fields and varies significantly with substorm activity driven by the solar wind [*Mauk and Meng*, 1983; *Kerns et al.*, 1994; *Liemohn et al.*, 1998; *Khazanov et al.*, 2004; *Ganushkina et al.*, 2013]. Inward electron transport excites plasma wave instabilities that give rise to local electron acceleration and electron precipitation into the atmosphere. Wave-particle interactions are very effective in precipitating electrons at energies of a few hundred keV, and radiation belt models often assume that losses are replenished by the transport of low-energy electrons from the plasma sheet [*Subbotin and Shprits*, 2009]. However, this is not a steady state process and this assumption is far from ideal.

At present, there are about 1000 operational satellites at different orbits in near-Earth space and all of them pass through the Earth's magnetosphere where the radiation environment can vary significantly with location [*Horne et al.*, 2013a]. The presence of low-energy electrons in GEO (geostationary) and MEO (medium Earth orbit) orbits mainly between midnight and dawn [*O'Brien*, 2009] can cause surface charging [*Purvis et al.*, 1984; *Whipple*, 1981; *Garrett*, 1981; *Davis et al.*, 2008], changes in the satellite potential, and degradation of satellite surface materials. Surface charging has been reported to cause anomalies on satellites on geosynchronous orbit [*Frezet et al.*, 1988; *Hoeber et al.*, 1998; *Lanzerotti et al.*, 1998; *Koons et al.*, 1999]. The injected electrons can also penetrate along the magnetic field lines to low altitudes and affect polar orbiting satellites in LEO (low Earth orbit) at high latitudes.

Fluxes of low-energy electrons have been modeled in several studies as a part of ring current simulations. *Jordanova and Miyoshi* [2005], *Miyoshi et al.* [2006], and, more recently, *Jordanova et al.* [2014] extended ring current-atmosphere interactions model (RAM) [*Jordanova et al.*, 1996] to relativistic energies and electrons investigating the effect of magnetospheric convection and radial diffusion during the October 2001 geomagnetic storm. *M. W. Chen et al.* [2006] performed magnetically self-consistent ring current simulations during the 19 October 1998 storm. These studies were focused on the application to specific events.

It is necessary to have a model that is able to specify the electron flux for all L shells and at all satellite orbits, when necessary for a given solar wind and IMF input. This model must also provide its output as an input for higher-energy radiation belt modeling. With the development of the Inner Magnetosphere Particle Transport and Acceleration Model (IMPTAM) [*Ganushkina et al.*, 2001, 2005, 2006, 2012a] for low-energy electrons in the inner magnetosphere [*Ganushkina et al.*, 2013] and operating it online under the SPACECAST project (http://fp7-spacecast.eu) [*Horne et al.*, 2013b] funded by the European Union Seventh Framework Programme (FP7/2007–2013), the computational view on the low-energy electron fluxes $L = 2$–10 is now feasible. In this paper, we present a nowcasting near-real-time model of low-energy electrons (<200 keV) in the inner magnetosphere and its operational implementations (sections 2 and 3). We use the real-time geostationary data from GOES 13 and GOES 15 satellites on the <200 keV electron fluxes to validate the running of IMPTAM online and show the comparisons in section 4. We summarize the model performance and the obtained results in section 5.

2. Nowcasting Procedure

The IMPTAM [*Ganushkina et al.*, 2001, 2005, 2006, 2012a] for low-energy electrons in the inner magnetosphere [*Ganushkina et al.*, 2013] is currently operating online and is driven by the following parameters provided in real time by the data acquisition procedure in SPACECAST:
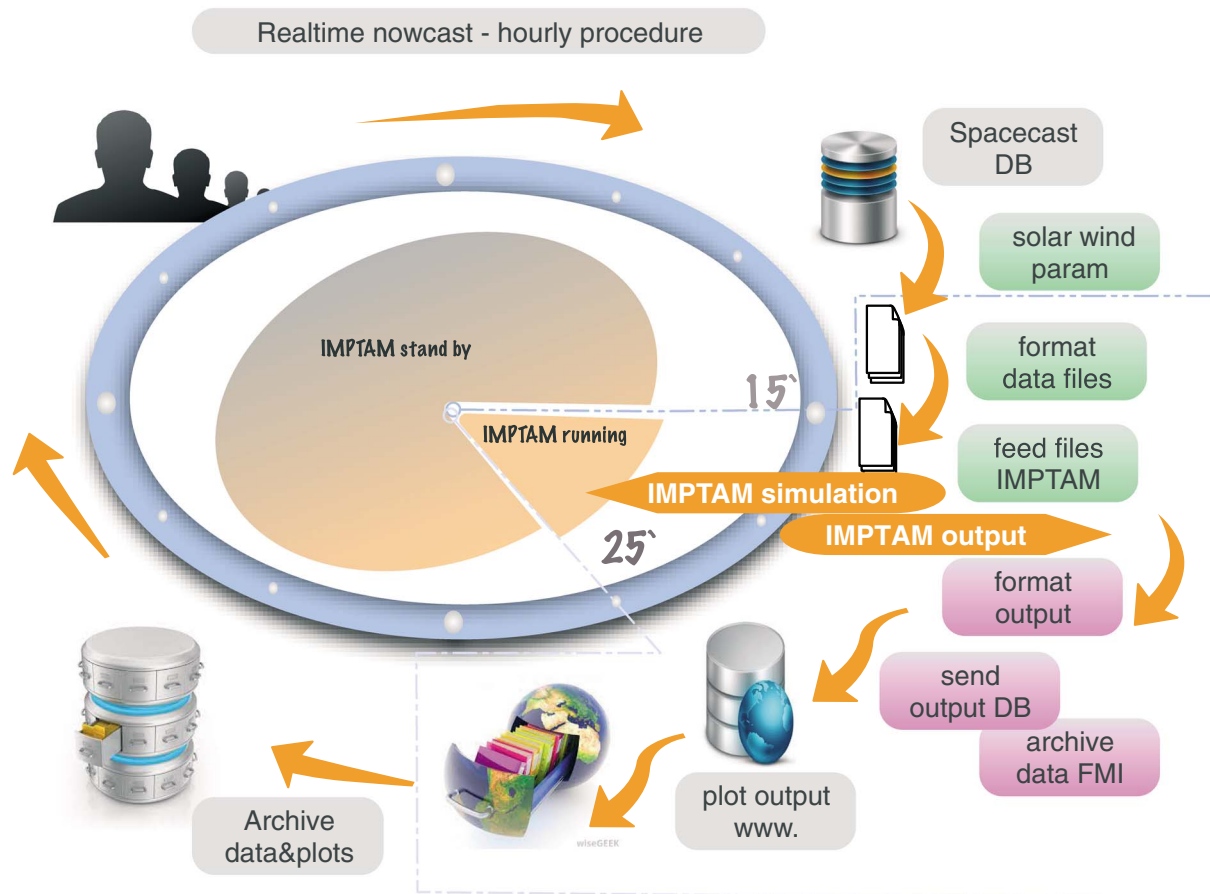
Figure 1. Schematic representation of the hourly procedure of running IMPTAM for the nowcast of low-energy electron fluxes in the inner magnetosphere. Color coded in green is "Cron-one" and in pink "Cron-two".

1. one minute resolution data of solar wind number density, total plasma bulk velocity, and solar wind dynamic pressure (NOAA Space Weather Prediction Center);
2. one minute resolution data of the interplanetary magnetic field (IMF) comprising three components in GSM coordinates (NOAA Space Weather Prediction Center); and
3. hourly values of the *Dst* index (compiled from NOAA National Geophysical Data Center and World Data Center for Geomagnetism, Kyoto).

All the data sources are freely available. The data files may contain times for which data are not available or filled with unrealistic numbers. When this happens to the *Dst* index, the values are assumed to be constant, so the last *Ds* value recorded in the local data files of parameters is used. During this period for solar wind and IMF parameters with 1 min resolution of the data, the values are ignored and the last proper values are kept constant through the data gap.

Figure 1 presents the general framework of the implemented nowcasting procedure with the most important steps for the internal and external links. The workflow is completely automated and does not need any manual interference from the user. The hourly, fully automated functioning of the nowcast is ensured by using the software utility "cron." Cron is a time-based job scheduler in Unix-like computer operating systems. This software has the ability, once set, to run periodically at fixed times, dates, or intervals scheduled jobs (commands or shell scripts) in specific software environments. Two cron jobs were implemented to ensure reliable and fully automated online operation. In Figure 1, the green color-coded boxes are "Cron-one" and pink color-coded boxes are "Cron-two." The first cron job (Cron-one) runs hourly at 15 min past the hour. Cron-one makes the following jobs automatic: (1) connecting to the external SPACECAST data acquisition system; (2) downloading four different files containing: solar wind and IMF parameters, *Dst* index and GOES data for comparison; (3) formatting the files for IMPTAM use; (4) checking if

IMPTAM is ready for new parameters; and (5) flagging IMPTAM that the data is ready to use. If on step (4) the state diagnoses determines that IMPTAM has stopped running for any reason, Cron-one can immediately restart IMPTAM from the last saved output. IMPTAM has the ability to save the output fluxes in the modeling domain at certain user-defined moments in time. These output fluxes serve as backups and constitute snapshots of the whole inner magnetosphere. Once a certain output flux is loaded, the simulation resumes. The second automated job (Cron-two) runs hourly at 25 min past the hour, allowing IMPTAM 10 min to process and simulate 1 h worth of data. Cron-two is responsible for (1) checking if IMPTAM has finished the simulation; (2) formatting the output in an easy to plot format; (3) connecting to an external ftp and upload the latest files; and (4) locally archiving the latest results. The output files are downloaded from the ftp and immediately made available in figure and tabular format on the SPACECAST website.

3. Modeling of Low-Energy Electrons With IMPTAM

The IMPTAM traces distributions of ions and electrons in the drift approximation with arbitrary pitch angles from the plasma sheet to the inner L shell regions with energies reaching up to hundreds of keVs in time-dependent magnetic and electric fields. One of the important results obtained from IMPTAM modeling is the ability of the model to reproduce the observed amount of ring current protons with energies > 80 keV during a storm recovery phase [*Ganushkina et al.*, 2006] by the addition of substorm-associated electromagnetic fields, which was not possible to obtain by other models using a dipole model for magnetic field and large-scale convection electric field. IMPTAM has been successfully used to examine the evolution of the current systems during magnetic storms [*Ganushkina et al.*, 2012a], to compute energetic ion drifts in the inner magnetosphere, and to evaluate the magnetospheric sources of magnetic disturbances recorded on the ground [*Ganushkina et al.*, 2012b] (i.e., the sources of the *Dst* index). The detailed description of IMPTAM was given in *Ganushkina et al.* [2005, 2012a] with the description for modeling of electrons in *Ganushkina et al.* [2013, 2014]. Here we will briefly repeat the main steps for modeling low-energy electrons in the inner magnetosphere.

We obtain the changes in the electron distribution function $f(R, \phi, t, E_{kin}, \alpha)$, where R and ϕ are the radial and azimuthal coordinates in the equatorial plane, respectively, t is the time, E_{kin} is the particle energy, and α is the particle pitch angle, considering the drift velocity as a combination of the $\mathbf{E} \times \mathbf{B}$ drift velocity and the velocities of gradient and curvature drifts [*Roederer*, 1970]. We assume the first and second adiabatic invariants to be constant and use the bounce average drift velocity after averaging over one bounce of $\mathbf{E} \times \mathbf{B}$ magnetic drift velocities. Liouville's theorem is used to gain information of the entire distribution function with losses taken into account. If we know the distribution function $f(R, \phi, t, E_{kin}, \alpha)$ of particles at a time moment t_1, then we can obtain the distribution function of particles at a time moment $t_2 = t_1 + \Delta t$, by computing the drift velocity of the particles. Since we need to take into account the phase-space-dependent losses (τ_{loss}), the final distribution function at t_2 will be $f(t_2) = f(t_1) \exp(-\Delta t / \tau_{loss})$.

For the obtained distribution function, we apply radial diffusion [*Fälthammar*, 1965; *Schulz and Lanzerotti*, 1974; *Brautigam and Albert*, 2000] by solving the radial diffusion equation [*Schulz and Lanzerotti*, 1974] for the distribution function. *Kp*-dependent radial diffusion coefficients D_{LL} for the magnetic field fluctuations are computed following *Brautigam and Albert* [2000] using $D_{LL} = 10^{0.056Kp-9.325}L^{10}$. Since diffusion by the magnetic field fluctuations at L > 3 dominates diffusion produced by electrostatic field fluctuations [*Shprits and Thorne*, 2004], we ignore the electrostatic component of the radial diffusion coefficient [*Lejosne et al.*, 2013]. After that, we repeat the order of calculation: first, we solve transport with losses and then apply the diffusion.

For electron losses we consider convection outflow and pitch angle diffusion by introducing the electron lifetimes. We use *Chen et al.* [2005] electron lifetimes for the strong diffusion and *Shprits et al.* [2007] electron lifetimes for the weak diffusion regimes.

An advantage of IMPTAM is that it can utilize any magnetic or electric field model, including a self-consistent magnetic field. In the model version running online in near-real time we use the set of models which was found to provide best agreement with the measured low-energy electron fluxes at geostationary orbit [*Ganushkina et al.*, 2013]. This set includes

1. a dipole model for the internal magnetic field,

2. T96 model [*Tsyganenko*, 1995] for the external magnetic field with Dst, P_{sw}, IMF B_y and B_z as input parameters, and

3. *Boyle et al.*'s [1997] polar cap potential dependent on solar wind and IMF parameters applied to a Volland-Stern type convection electric field pattern.

As for including the self-consistency, we estimate its effect to be small. IMPTAM can take into account the self-consistency of the magnetic field by calculating the magnetic field produced by the model currents and feeding it back to the background magnetic field. It is necessary to be careful when calculating a self-consistent magnetic field using a realistic model magnetic field such as Tsyganenko models. These models contain the prescribed ring and near-Earth tail currents. If they are used together with calculations of the induced magnetic field to trace particles in them, the obtained results will be incorrect. To be accurate, it is necessary to remove the model ring and near-Earth tail currents from the background magnetic field model and consider self-consistent calculations of the magnetic field. In previous calculations on this subject [*Ganushkina*, 2011], it has been shown that the Tsyganenko models produce a near-Earth nightside field that is relatively close to the field distortions from self-consistent magnetic field calculations. This is because of the $1/r^2$ dependence of the magnetic perturbation relative to its associated current density. Therefore, even if current systems are highly localized, the resulting magnetic field distortion is fairly smooth and well captured by the empirically derived current configurations within the Tsyganenko models. Since we study the electrons, their contribution to the ring current is no more than 10%, so their contribution to the distortion of the background magnetic field is small. Moreover, at the distances from 10 to 6.6 R_E, the effect of the electron-pressure-driven self-consistent magnetic field is expected to be small.

There are large asymmetries in magnetic field and particle data of the inner magnetosphere in the region of ring current. Around this region of high-pressure flows, a current is primarily closing through field-aligned currents and the ionosphere, altering the near-Earth electric potential pattern [*Jaggi and Wolf*, 1973; *Ridley and Liemohn*, 2002]. Taking into account the electric field in a self-consistent way is of high importance when modeling the inner magnetosphere particles [*Fok et al.*, 2003; *Liemohn and Brandt*, 2005]. In our study we focus on low-energy electrons which do not contribute significantly to the total pressure as compared to ions. In addition, when these electrons precipitate into the upper atmosphere, they create the high-conductance area of the auroral oval and their feedback on the electric field is short-circuited by this precipitation. Therefore, electric field self-consistency is not needed to accurately describe the flow of electrons through the near-Earth nightside magnetosphere. For the nowcast online model, the electrons are moved in the *Boyle et al.* [1997] electric field and its alterations by the electron-driven field-aligned currents and precipitating electrons are considered small.

We set the model boundary at 10 R_E and use the kappa electron distribution function $f_k(E) = n \cdot (\frac{m}{2\pi kE_0^*})^{3/2} \cdot \frac{\Gamma(k+1)}{\Gamma(k-1/2)} \cdot (1 + \frac{E}{kE_0^*})^{-(k+1)}$, where Γ is the Gamma function. Analysis of early measurements of plasma sheet particles in the Earth's magnetosphere [*Vasyliunas*, 1968; *Christon et al.*, 1989, 1991] and more recent studies on Geotail and Cluster observations [*Åsnes et al.*, 2008; *Burin des Roziers et al.*, 2009] found that the typical energy spectra fits best by a kappa distribution with spectral slopes in the range $k = 4$–8. In the beginning of online simulation in March 2013, we started with $k = 5$. Our previous results presented as a part of the review paper by *Horne et al.* [2013b] (see section 3 and Figure 3) pointed out that decreasing k parameter from 5 to 1.5 provided the best agreement between the modeled and the observed electron fluxes with 50–150 keV energies at geostationary orbit onboard LANL satellite.

The k values lower than in earlier studies were recently obtained based on the analysis of Cluster ($k = 2.89$ for the single component fits of the observed electron distribution [*Walsh et al.*, 2013]) and The Time History of Events and Macroscale Interactions during Substorms (THEMIS) ($k = 2.5$–3 for 40 keV electrons during injection events [*Gabrielse et al.*, 2014]) data. It may seem that k values lower than 2 can cause a divergence of the integration when we obtain, for example, the omni directional energy flux following *Vasyliunas* [1968] (equation (11c)). In our model, we assume that the distribution can be fitted by the kappa shape only in the finite range of velocities, so the integral does not diverge.

We then changed it $k = 1.5$ at the end of the year after continuous monitoring of the model output compared to GOES data (see the next section). Particle energy at the distribution peak E_0^* is given by $E_0^* = k_B T(1 - 3/2k)$. Particle flux on the outer boundary is given by $j_k(E) = n \cdot \frac{2\sqrt{m}}{m} \cdot (\frac{1}{2\pi k})^{3/2} \cdot \frac{E}{(E_0^*)^{3/2}} \cdot \frac{\Gamma(k+1)}{\Gamma(k-1/2)} \cdot (1 + \frac{E}{kE_0^*})^{-(k+1)}$. The number density n and temperature T are given by the empirical model derived from
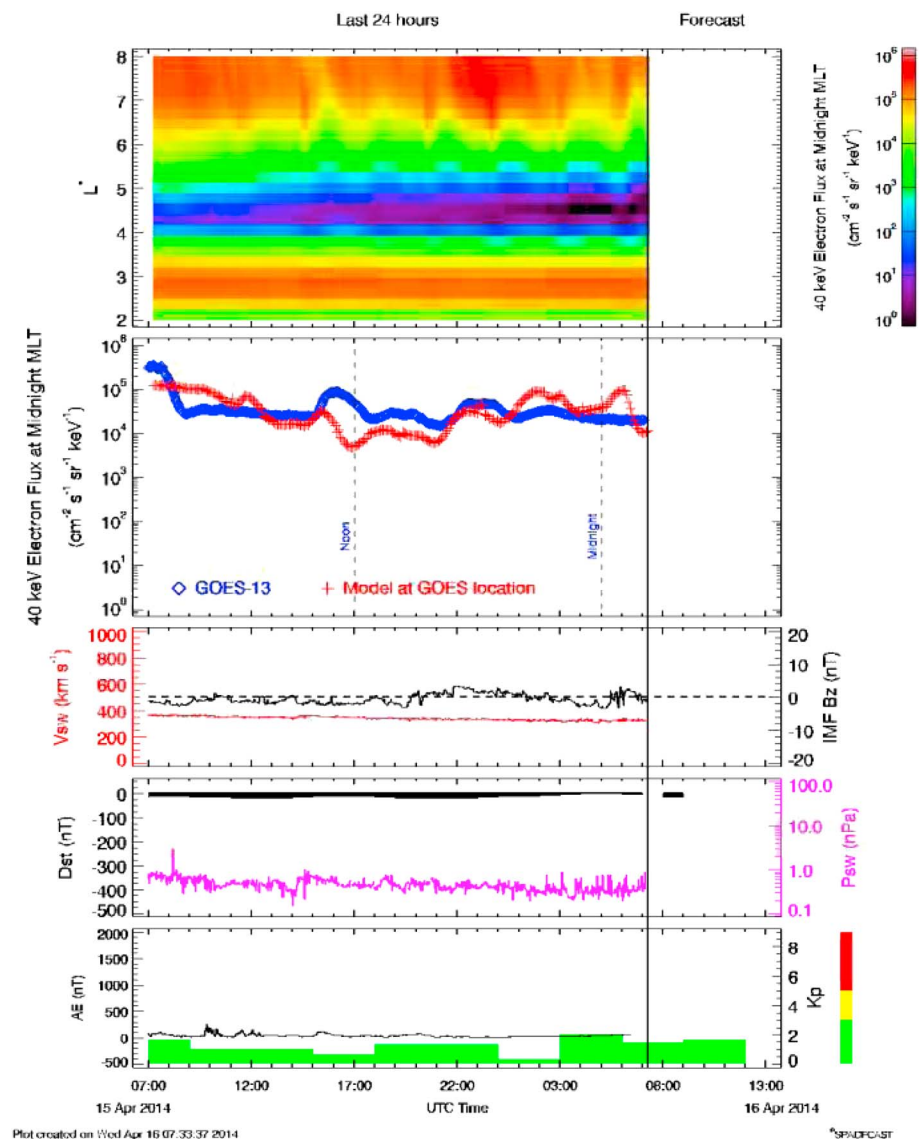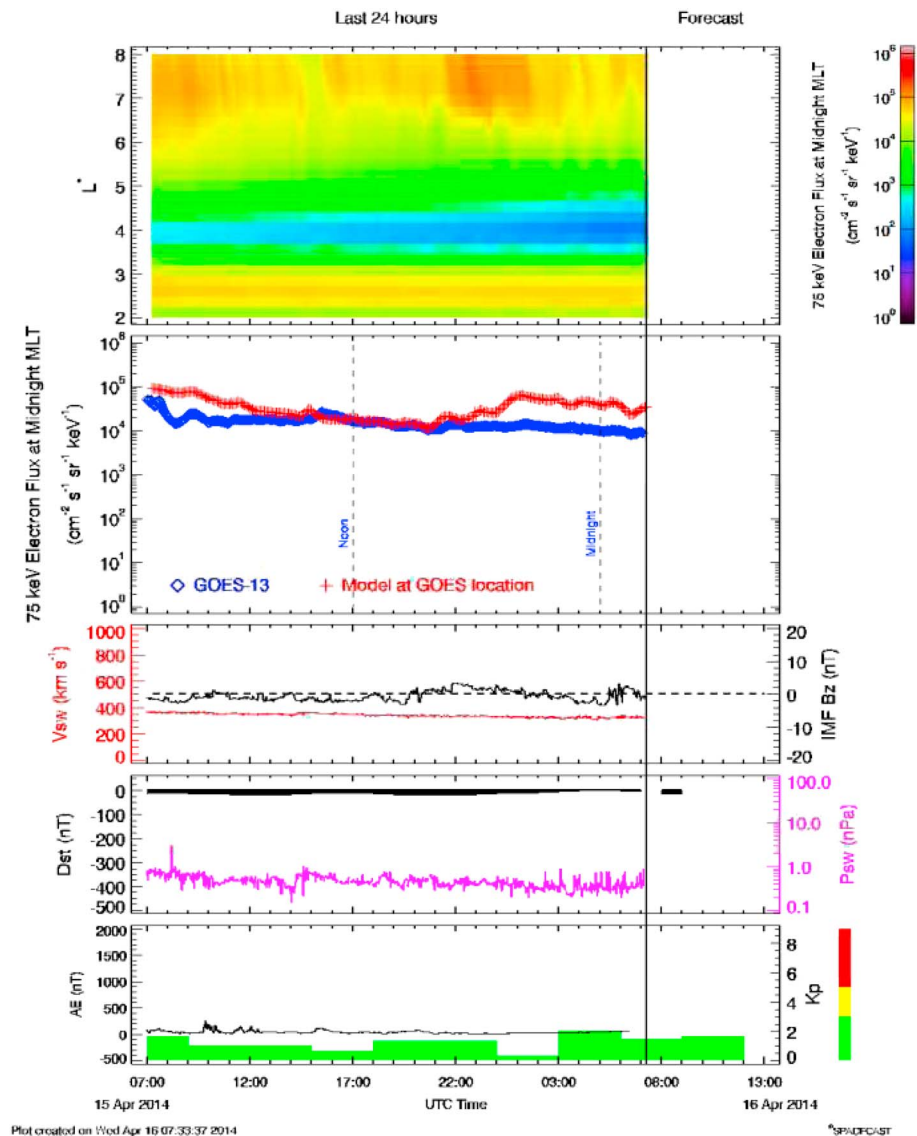
Figure 2. Example of low-energy electrons' nowcast during 15 April 2014, 0700 UT to 16 April 2014, 1900 UT: From top to bottom: (first panel) The 30–50 keV electron flux at $L = 2 - 8$ at midnight, (second panel) the 40 keV electron flux measured at GOES 13 (blue diamonds) together with the model flux (red pluses), (third panel) the IMF B_z component (black curve) and the solar wind velocity (red curve), (fourth panel) the solar wind dynamic pressure (magenta curve) and the Dst index (black curve), and (fifth panel) the Kp (green-yellow-red color bar) and AE indices (black curve).

Geotail data by *Tsyganenko and Mukai* [2003]. The electron n is assumed to be the same as that for ions in the model, but Te/Ti = 0.2 is taken into account (as was shown, for example, in *Kaufmann et al.* [2005] and *Wang et al.* [2012], based on Geotail and THEMIS data). We also introduced a time shift of 2 h following *Borovsky et al.* [1998] for the solar wind material to reach the midtail plasma sheet.

4. Online Nowcast for Low-Energy Electrons
4.1. Model Snapshots for 24 h
The online nowcast for low-energy electrons is presented at http://fp7-spacecast.eu web page under the SPACECAST project funded by the European Union Seventh Framework Programme (FP7/2007-2013). We show the results for three electron energy ranges, namely, 30–50 keV, 50–100 keV, and 100–200 keV, which correspond to the low-energy electron energy channels on Magnetospheric Electron Detector (MAGED) onboard the GOES satellites starting from GOES 13 (see GOES N data book, prepared for National Aeronautics and Space Administration, Goddard Space Flight Center, Greenbelt, Maryland 20771, Pursuant
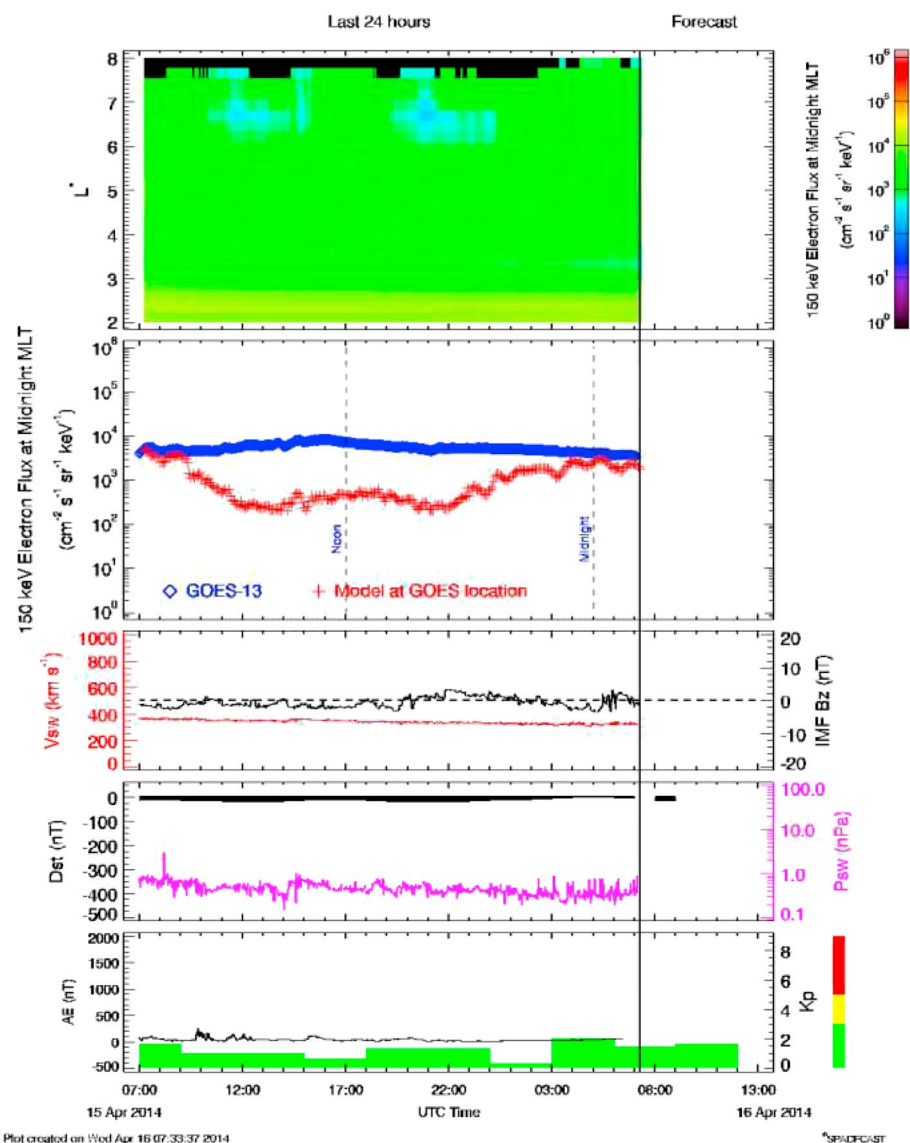
GANUSHKINA ET AL. 21

Figure 3. Example of low-energy electrons' nowcast during 15 April 2014, 0700 UT to 16 April 2014, 1900 UT for 50–100 keV (75 keV) (same as in Figure 2).

to Contract NAS5-98069, Rev B, February 2005, CDRL PM-1-1-03, Boeing, unpublished work, 2006). The GOES MAGED data in these three energy channels are the only available real-time data set for low-energy electrons. We present the results in the same format as they appear online.

Starting from GOES 13, the Space Environment Monitor (SEM) subsystem on GOES spacecraft consists of multiple instruments used to monitor the near-Earth (geostationary altitude) space environment including the EPS (Energetic Particle Sensor)/HEPAD (High Energy Proton and Alpha Detector) Instrument. It measures the flux of protons, alpha particles, and electrons over an extensive range of particle energies. One of the constituents of this instrument is the MAGED detector. Magnetospheric electrons are measured at nine pitch angle directions. The detector set is mounted on the anti-Earth side of the spacecraft and measures electrons at 0°, ±35°, and ±70° from the anti-Earth direction in both the equatorial and the azimuthal planes. Each detector telescope has a full detection cone angle of 30°. MAGED measures electrons in five differential energy channels from 30 to 600 keV. Algorithms are provided to correct the electron channels for the proton contamination that is unavoidable with this detection system.

For comparison with GOES MAGED data online, we use the data from the central telescope (telescope 1) facing in the zenith direction and covering mostly 90° pitch angles. Figures 2–4 demonstrate one example
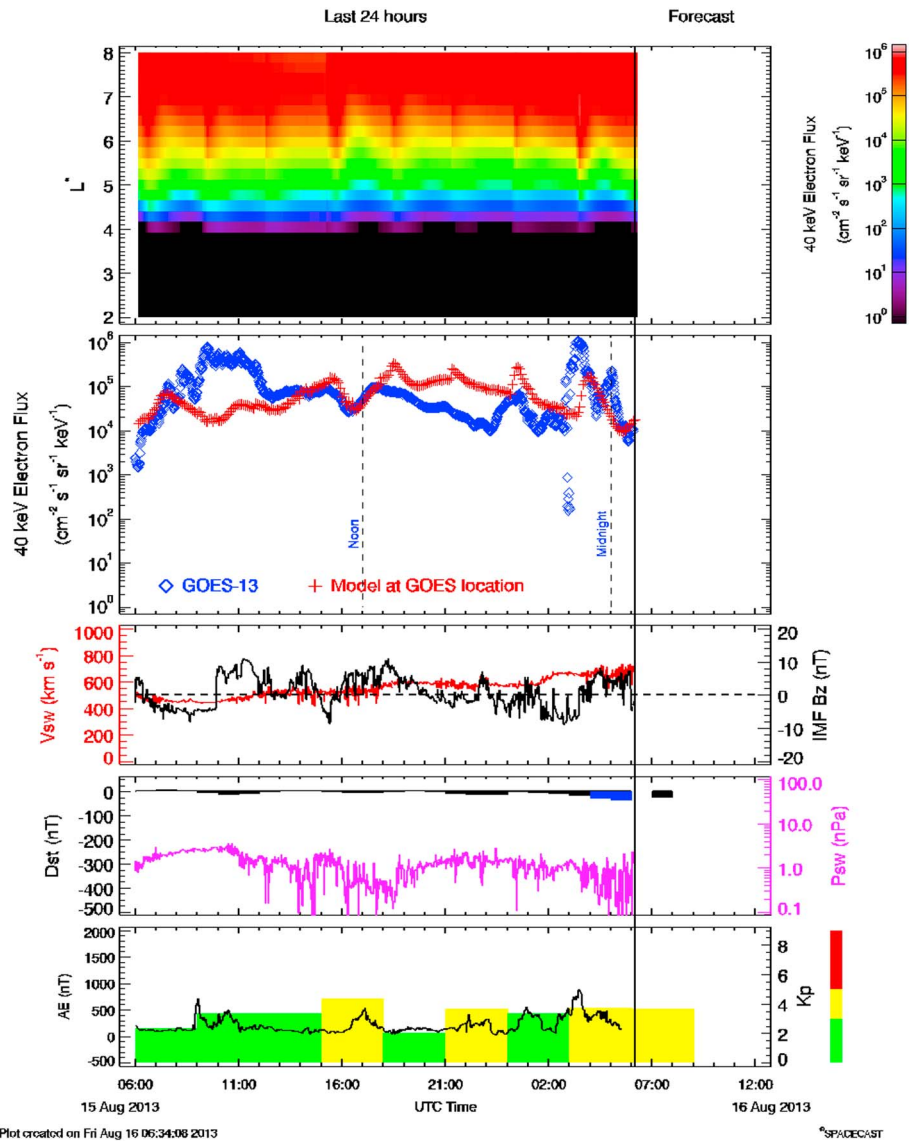
Figure 4. Example of low-energy electrons' nowcast during 15 April 2014, 0700 UT to 16 April 2014, 1900 UT for 100–200 keV (150 keV) (same as in Figure 2).

of the model output for low-energy electrons model as presented at http://fp7-spacecast.eu web page as 24 h snapshots for 15 April 2014, 0700 UT to 16 April 2014, 1900 UT. Figure 2 contains the results for electrons with energies of 40 keV. Figure 3 corresponds to the electrons with energies of 75 keV, and Figure 4 for 150 keV electrons. The first panel in Figures 2–4 shows the time evolution of the electron flux in $cm^{-2} s^{-1} sr^{-1} keV^{-1}$ at $L = 2 - 8$ at midnight. The second panel presents the electron flux measured at GOES 13 by telescope 1 (blue diamonds) during this time interval together with the model flux (red pluses) for corresponding energy at the GOES orbit. The satellite midnight and noon locations are marked by dashed vertical lines. The IMF B_z component (black curve) and the solar wind velocity (red curve) are shown on the third panel, the solar wind dynamic pressure (magenta curve) and the Dst index (black curve), on the fourth panel, and the Kp (green-yellow-red color bar) and AE indices (black curve), on the fifth panel.

The presented time period was rather quiet, IMF B_z being about −4 nT until 2000 UT on 15 April turning then northward with 2 nT and becoming negative again at 0100 UT on 16 April. Solar wind velocity was around 400 km/s, solar wind dynamic pressure did not rise above 1 nPa, no significant activations were seen in AE index, Kp was below or at about 2 and Dst did not drop lower than −10 nT. The modeled and observed electron fluxes show rather reasonable agreement on average for all three energy ranges. The flux of 40 keV
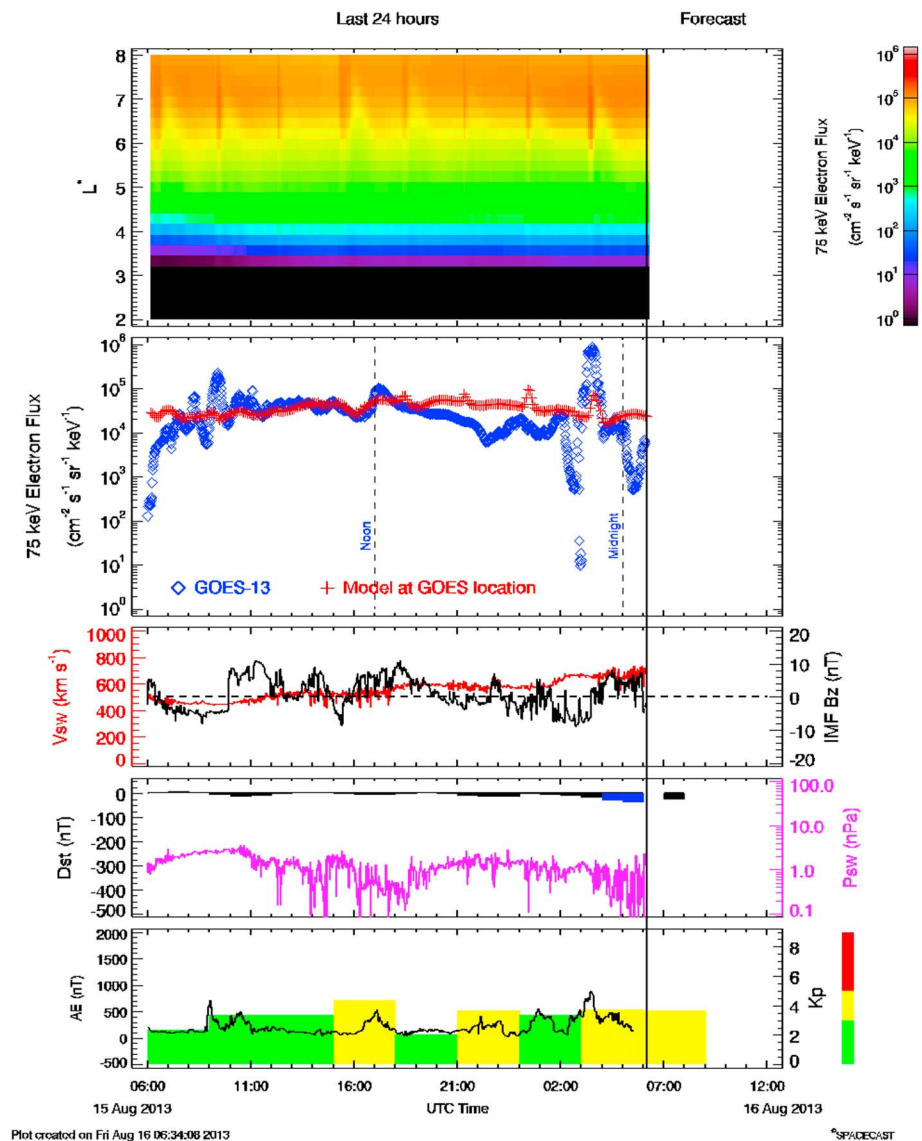
Figure 5. Example of low-energy electrons' nowcast during 15 August 2013, 0600 UT to 16 August 2013, 0700 UT for 30–50 keV (40 keV) electrons (same as in Figure 2).

electrons (Figure 2) shows most variations compared to the fluxes for 75 and 150 keV electrons. In the beginning of the presented time interval, GOES 13 was moving toward noon on 15 April, and the 40 keV modeled and observed fluxes were very close being about 3–$4 \cdot 10^4$ cm^{-2} s^{-1} sr^{-1} keV^{-1}. At noon at 1700 UT the modeled flux was an order of magnitude lower than the observed one. Then satellite moved to the duskside and the modeled fluxes were very close again to the observed values. At 0500 UT on 16 April, GOES 13 reached midnight and the modeled and observed fluxes coincided very well. For 75 keV electrons the agreement is also very good although it is necessary to mention that no significant variations were observed. The observed flux stayed at the level of 1–$2 \cdot 10^4$ cm^{-2} s^{-1} sr^{-1} keV^{-1}. The modeled flux was very close to the observed values when GOES 13 moved toward noon but became about 4 times higher than that observed when GOES 13 was coming to midnight through dusk. At the same time, the higher energy flux (150 keV) was observed at 10^4 cm^{-2} s^{-1} sr^{-1} keV^{-1} level but the modeled flux was close to the observed only around midnight and was lower being about $5 \cdot 10^2$ cm^{-2} s^{-1} sr^{-1} keV^{-1} at other local times.

Another example of nowcast output is for more disturbed conditions during 15 August 2013, 0600 UT to 16 August 2013, 0700 UT (Figures 5–7). In the beginning of 15 August, IMF B_z was varying around zero and then stayed negative from 0600 to 1000 UT turning positive at that time and reaching 10 nT. Solar wind
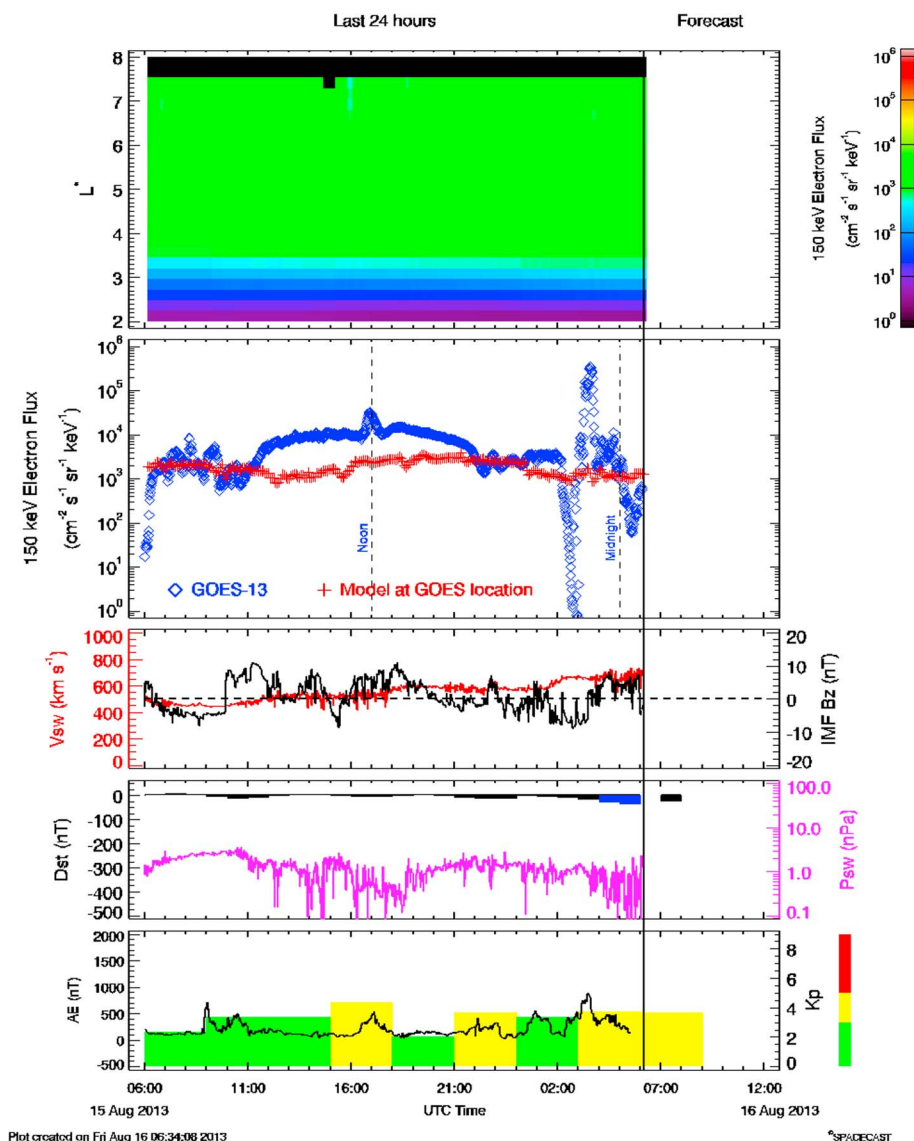
Figure 6. Example of low-energy electrons' nowcast during 15 August 2013, 0600 UT to 16 August 2013, 0700 UT for 50–100 keV (75 keV) (same as in Figure 2).

speed was about 500 km/s, solar wind dynamics pressure was around 3–4 nPa, $Kp = 3$, Dst was about −5 nT, and AE showed substorm activations with 800 nT around 0900 UT.

At that time GOES 13 was moving from midnight toward noon through dawn. The observed 40 keV electron flux was very well reproduced by the model in the beginning of this period (Figure 5). Later on it showed an increase with a peak of two orders of magnitude around 0930 UT, which was not reproduced by the model. This increase of the observed fluxes at dawn is most probably associated with possible substorm injections as presence of substorm activations was seen in AE. Electron fluxes with energies of 75 keV (Figure 6) and 150 keV (Figure 7) showed smaller variations during that period, and the modeled fluxes were about $3 \cdot 10^4$ cm^{-2} s^{-1} sr^{-1} keV^{-1} for 75 keV and $2 \cdot 10^3$ cm^{-2} s^{-1} sr^{-1} keV^{-1} for 150 keV which fits the data on average.

When satellite was around noon, the modeled fluxes for < 100 keV electrons matched the observed ones very well. IMF B_z became negative and reached −10 nT at 1530 UT. For higher-energy electrons (100–200 keV), the model underestimated the observed fluxes by almost an order of magnitude.

Contrary to the dawnside, the model fluxes for 40 keV electrons were several times higher than the observed ones on duskside. This difference decreased noticeably (starting from 0100 UT on 16 August) when GOES

Figure 7. Example of low-energy electrons' nowcast during 15 August 2013, 0600 UT to 16 August 2013, 0700 UT for 100–200 keV (150 keV) (same as in Figure 2).

13 came closer to midnight. During that time, the observed peak of 10^6 cm^{-2} s^{-1} sr^{-1} keV^{-1} at 0330 UT was seen in the model as 1 order of magnitude lower peak 30 min later. A second peak at 0600 UT at midnight was not reproduced by the model, but the model flux followed the observed one very well, on average. The flux variations seen for higher energies (Figures 6–7) were not reproduced by the model, but the modeled fluxes were of the same order of magnitude with the observed ones, on average. During that time, several excursions of negative IMF B_z were present with indications of substorm activity seen AE.

4.2. Model Performance
4.2.1. Direct Long-Term Data-Model Comparison
The IMPTAM version for low-energy electrons has been running online since March 2013. Constant checks were done for model performance. In Figure 8 we present the model output for 1 month, from 6 July to 8 August 2013. Figure 8 shows the observed fluxes (black lines) at GOES 13 together with the modeled fluxes for (a) 40 keV electrons (red line), (b) 75 keV electrons (blue line), and (c) 150 keV electrons (green line).

The general trends for deviations of the modeled fluxes from the observed ones as found for day long model outputs (Figures 2–4) can be seen for model performance over 1 month. The modeled fluxes for $< 100 keV$ electrons are, on average, in satisfactory agreement with the observed fluxes (Figures 8a and 8b). At the

July 6 - August 8, 2013
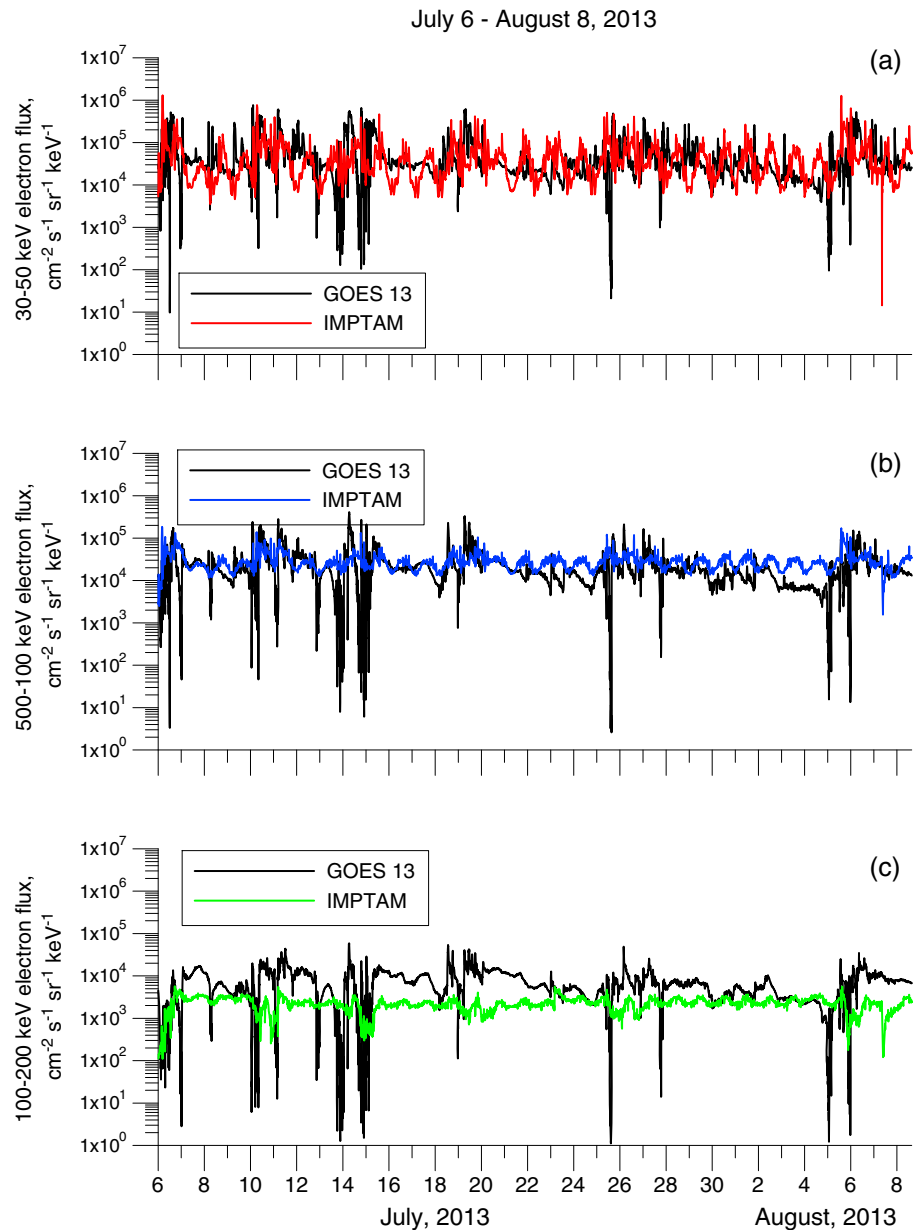
Figure 8. Model performance for 1 month, from 6 July to 8 August 2013: the observed fluxes (black lines) at GOES 13 together with the modeled fluxes for (a) 40 keV electrons (red line), (b) 75 keV electrons (blue line), and (c) 150 keV electrons (green line).

same time, the significant flux dropouts were not present in the model fluxes. For electrons with energies of 150 keV (Figure 8c), the modeled flux is constantly smaller than the observed one. The maximum difference between the observed and modeled fluxes can reach 1 order of magnitude.

Figure 9 presents the long-term data-model comparison, same as in Figure 8 but for 4 months, from 1 January to 30 April 2014. During this period, the k was 1.5 in the kappa distribution function at the boundary in the plasma sheet. At a first glance, the model performance for 1 month is very similar to that for 4 months. At the same time, it can be noticed that the model follows the observations more closely, which will be demonstrated below. Several gaps in the model output can be noticed. They are due to IMPTAM's restarts which have occurred 6 times during that period. The IMPTAM was forced to restart the modeling with empty magnetosphere mainly by internal problems of ftp server. The periods when the initial filling
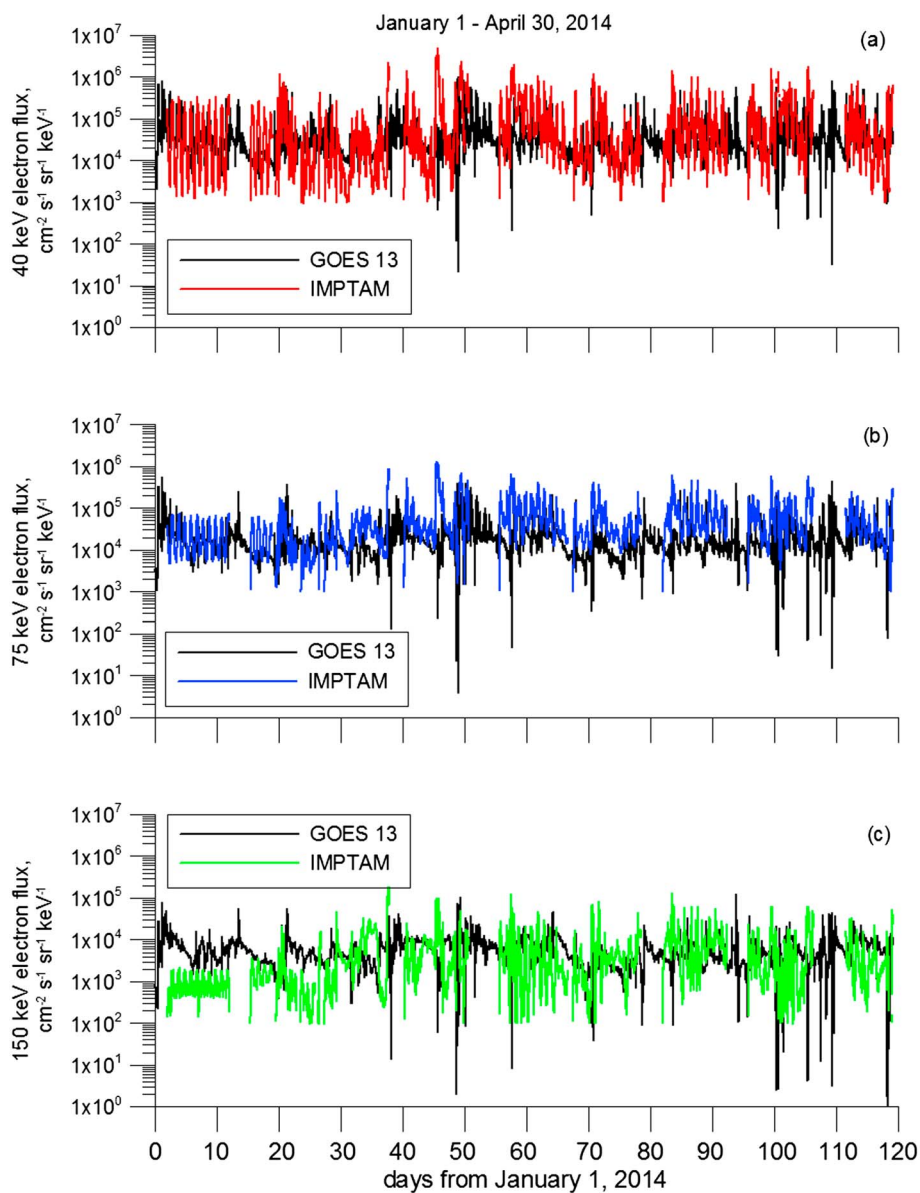
Figure 9. Model performance, same as in Figure 8 but for 4 months, from 1 January to 30 April 2014.

of the magnetosphere was going on and the model flux values were very small were excluded from the model-data comparison.

4.2.2. Nowcast Verification

The accumulated output from IMPTAM online at GOES satellite locations was evaluated. As a first step, we chose the root-mean-square deviation (RMSD) or root-mean-square error (RMSE), which is a frequently used measure of the differences between values predicted by a model or an estimator and the values actually observed. These individual differences are called residuals when the calculations are performed over the data sample that was used for estimation. They are called prediction errors when computed out of sample. The RMSD serves to aggregate the magnitudes of the errors in predictions for various times into a single measure of predictive power. RMSD is a good measure of accuracy, but it can be used only to compare forecasting errors of different models for a particular variable and not between variables, as it is scale-dependent.

Table 1. Normalized Root-Mean-Squared Deviation (NRMSD) and the Associated Standard Deviations of the Observations (Parenthetical; in Units of cm^{-2} s^{-1} sr^{-1} keV^{-1})[a]

| | Energy Channel | | |
	40 keV	75 keV	150 keV
Jul–Aug 2013	1.3016(7.901E+04)	1.0262(3.052E+04)	1.3577(5.645E+03)
Jan–Apr 2014	0.0324(8.288E+04)	0.0153(3.438E+04)	0.0307(5.737E+03)

[a]Two time periods are shown: 6 July to 8 August 2013 (top row) and 1 January to 30 April 2014 (bottom row).

RMSD is used to compare differences between two things that may vary, neither of which is accepted as the "standard." For example, when measuring the average difference between two time series $x_{1,t}$ and $x_{2,t}$, the formula becomes

$$\text{RMSD} = \sqrt{\frac{\sum_{t=1}^{n} (x_{1,t} - x_{2,t})^2}{n}} \tag{1}$$

Note that if an unskilled prediction is made using the mean of the distribution of observed values (μ_{obs}, replacing x_2 above), equation (1) becomes the standard deviation of the observed values. Normalized RMSD can be generated by dividing RMSD by some measure of the distribution of the observed values (the range of the observations is often used). For this study, NRMSD (equivalently, NRMSE) is obtained by dividing RMSD by the standard deviation of the observed values:

$$\text{NRMSD} = \frac{\text{RMSD}}{\sigma_{obs}} \tag{2}$$

This choice of normalization has several advantages. First, because the flux values being examined span many orders of magnitude, the normalization scheme must be robust against large magnitude outliers. Standard deviation is more robust than the mean or range of the observations. Additionally, because the RMSD resulting from a constant prediction of μ_{obs} is equivalent to σ_{obs}, NRMSD of a prediction of μ_{obs} is 1. Thus, it is expected that a skilled prediction would yield an NRMSD below 1 (average error is within a single standard deviation of the observations) and an unskilled prediction would yield an NRMSD well above 1.

Table 1 shows the results of this calculation for two time periods. Periods directly following model restarts, where fluxes were built up from zero to realistic values, were disregarded. For the test, 1 month performance for 6 July to 7 August 2013 (Figure 8), we obtained NRMSD values slightly higher than unity for each energy channel. For online IMPTAM performance during first 4 months in 2014 (Figure 9, we obtained much lower values, ranging from 0.015 to 0.0324. Though these metrics are buoyed by large standard deviations owing to the dynamic nature of the fluxes, they demonstrate that IMPTAM, on average, does reasonably well predicting flux magnitudes. Additionally, between the two modeling time periods, tuning of our model improved overall performance.

Another approach which we used is binary event tables [*Jolliffe and Stephenson*, 2003]. These predictions are considered as yes/no forecast within a given time interval and represent the simplest type of forecasting and decision-making. There are two ways for a forecast to be correct (either a Hit or a Correct Rejection) and two ways for a forecast to be incorrect (either a False Alarm or a Miss). In practice, many sets of binary forecasts are produced by varying a threshold. A Hit and a False Alarm count is made if the model can or cannot forecast a certain threshold. To evaluate the model performance, several thresholds are needed.

The main metric is the Heidke Skill Score (HSS), which is determined as

$$\text{HSS} = \frac{2s(1-s)(H-F)}{s + s(1-2s)H + (1-s)(1-2s)F}, \tag{3}$$

where

$$s = \frac{\text{Hit} + \text{Miss}}{\text{Sum of all events}} \tag{4}$$

is the event probability (base rate),

$$H = \frac{\text{Hit}}{\text{Hit} + \text{Miss}} \tag{5}$$

Table 2. IMPTAM Performance Determined From the Binary Event Tables for 1 Hour Window in the Time-Dependent IMPTAM Output With 2201 Events in Total

Flux Level, (cm^{-2} s^{-1} sr^{-1} keV^{-1})	Hit	False Alarm	Miss	Correct Rejection	Hit Rate	False Alarm Rate	Heidke Skill Score
			40 keV Electron Fluxes				
5 ·10^4	348	721	179	953	0.660	0.431	0.170
1 ·10^5	109	612	121	1359	0.474	0.311	0.084
2 ·10^5	34	403	73	1691	0.318	0.192	0.051
3 ·10^5	16	288	39	1858	0.291	0.134	0.049
4 ·10^5	5	228	22	1946	0.185	0.105	0.017
			75 keV Electron Fluxes				
3 ·10^4	295	1043	104	759	0.739	0.579	0.084
5 ·10^4	82	816	85	1218	0.491	0.401	0.030
1 ·10^5	18	429	31	1723	0.367	0.199	0.034
			150 keV Electron Fluxes				
3 ·10^3	34	403	73	1691	0.485	0.603	−0.077
3.5 ·10^3	16	288	39	1858	0.438	0.525	−0.065
1 ·10^4	5	228	22	1946	0.159	0.233	−0.064

is the Hit Rate and

$$F = \frac{\text{False Alarm}}{\text{False Alarm} + \text{Correct Rejection}} \tag{6}$$

is the False Alarm Rate. The perfect skill gives HSS = 1, the minimum value is −1.

For IMPTAM output we selected several thresholds of the values of the electron fluxes depending on the electron energy shown in Table 2. We computed the binary event tables for 1 h window (Hit, False Alarm, Miss, Correct Rejection) in the time-dependent IMPTAM output for 4 months (1 January to 30 April 2014) and determined the Hit Rates, the False Alarm Rates, and the Heidke Skill Scores. The total number of all events was 2201.

It must be noted that significant flux dropouts were not present in the model fluxes. For 40 keV electrons, the difference between the observed and modeled fluxes is oscillating around zero. The 1 h window gives a rather small HSS but reasonable hit and false alarm rates for the first three thresholds. The best hit rate is for 75 keV electrons. The modeled fluxes of 150 keV electrons are constantly smaller than the observed ones (1 order of magnitude). Nevertheless, the hit rates are reasonable for 150 keV electrons, but the HSS is very small.

We present here the estimates of model performance for four first months of 2014, since the model output corresponds to the most correct set of models in IMPTAM including $k = 1.5$ for boundary distribution. We must stress that this is the first attempt to model low-energy electrons in real time at 10 min resolution. The basic level of the observed fluxes is reproduced. We have developed a very powerful tool, and the model performance will be improved with our next efforts on model development.

5. Summary and Discussion

We presented the nowcast model for low-energy (< 200 keV) electrons in the inner magnetosphere, operating online in near real time under the SPACECAST project (http://fp7-spacecast.eu), which is the version of the Inner Magnetosphere Particle Transport and Acceleration Model (IMPTAM) [*Ganushkina et al.*, 2001, 2005, 2006, 2012a] for electrons [*Ganushkina et al.*, 2013, 2014]. The presented model provides the low-energy electron flux at all L shells and at all satellite orbits, when necessary. The model is driven by the real time solar wind and IMF parameters with 1 h time shift for propagation to the Earth's magnetopause, and by the real-time *Dst* index. Real-time geostationary GOES 13 or GOES 15 (whenever available) MAGED data on electron fluxes in three energy channels (30–50 keV, 50–100 keV, and 100–200 keV) for three energies of 40, 75, and 150 keV are used for comparison and validation of IMPTAM running online. The GOES MAGED data in these three energy channels are the only available real-time data set for low-energy electrons. Long-term comparison with other data sets not available in real time at present, such as, HOPE [*Funsten et al.*, 2013] and MagEIS [*Blake et al.*, 2013] data in the range of 1 to 200 keV from ECT Instrument

Suite [*Spence et al.*, 2013] onboard Van Allen Probes, is a proper and necessary test to conduct for model performance which will be done in the near future.

At the same time, it is necessary to stress that the nowcast model is not the same as the model which can be used for specific scientific studies. When we run the model online, we need to have data which can be available in real time. We cannot go back and change the model settings or add other physical processes which could be missing to the model to fit the data better as we usually do for past event analysis. Adding comparisons to other data sets, not available in real time, will mean not a nowcast model but case studies. Thus, validation of online model performance is limited at present.

Another important thing is that it is hard to expect that a model working online in real time will capture all the variations in the observed fluxes. As was mentioned above, it is impossible to change the model parameters while it is working online to fit the data better. Thus, the model must be able to work well with a certain set of parameters during different geomagnetic conditions and in different regions of the inner magnetosphere and, moreover, on the 10 min or so time scales. It is a challenging task, and we presented our first attempts to deal with it.

At present, the nowcast for low-energy electrons are provided in near real time for three energy ranges (30–50 keV, 50–100 keV, and 100–200 keV) as (1) time evolution of the electron flux in cm^{-2} s^{-1} sr^{-1} keV^{-1} at L = 2–8 at midnight, and (2) as the electron flux for 40, 75, and 150 keV at the GOES 13 (or GOES 15) orbit together with the measured flux at GOES 13 (or GOES 15) by telescope 1. The IMF B_z, the solar wind velocity, solar wind dynamic pressure, *Dst* index, *Kp*, and *AE* indices are also provided.

On average, the model provides reasonable agreement with the data, the basic level of the observed fluxes is reproduced. The best agreement between the modeled and the observed fluxes are found for <100 keV electrons. At the same time, not all the peaks and dropouts in the observed electron fluxes are reproduced. For 150 keV electrons, the modeled fluxes are often smaller than the observed ones by an order of magnitude. The NRMSD is to range from 0.015 to 0.0324. The computed binary event tables for 1 h window reveal reasonable hit rates being 0.660–0.318 for flux thresholds of 5 ·10^4–2 ·10^5 cm^{-2} s^{-1} sr^{-1} keV^{-1} for 40 keV electrons, 0.739–0.367 for flux thresholds of 3 ·10^4–1 ·10^5 cm^{-2} s^{-1} sr^{-1} keV^{-1} for 75 keV electrons, and 0.485–0.438 for flux thresholds of 3 ·10^3–3.5 ·10^3 cm^{-2} s^{-1} sr^{-1} keV^{-1} for 150 keV electrons but rather small Heidke Skill Scores (0.17 and below). This is the first attempt to model low-energy electrons in real time at 10 min resolution. The output of this model can serve as an input of the electron seed population for the higher-energy radiation belt modeling.

As a result of the comparison of modeled fluxes to the GOES 13 observations over a 1 month period and 4 months period shown in the present paper, we found that some of the observed significant peaks and dropouts cannot be reproduced by the set of background magnetic and electric field models and boundary conditions used in IMPTAM. IMPTAM is driven by the variations in the solar wind and IMF via the dependence of the background magnetic and electric field models and boundary conditions on the solar wind number density, velocity, dynamics pressure, IMF components, and *Dst* index. If no significant variations are seen in these parameters, no observed peaks and dropouts can be represented.

The observed variations can be associated with substorm activity seen in the *AE* index. The large-scale background electric and magnetic fields used in IMPTAM for the presented near-real-time output do not have the effect of substorm variations. As was shown in *Ganushkina et al.* [2013, 2014], the substorm-associated electromagnetic fields are of key importance for the electron transport and acceleration from the plasma sheet to the inner magnetosphere. The effects which substorm activity has upon the transport and acceleration of low-energy electrons were incorporated by launching an electromagnetic pulse at substorm onset times determined from *AE* index variations. It is not a straightforward task to incorporate the substorm activity effects for nowcast modeling. To launch a pulse at a substorm onset, the substorm timing and *AE* peaks must be forecasted. If the forecasting tools for *AE* index are developed in the future, the substorm activity effects could be properly taken into account.

Another explanation for the discrepancy between the observed and modeled fluxes is the usage of the empirical model by *Tsyganenko and Mukai* [2003] as boundary conditions 10 R_E which was developed for ions. Applying this model for boundary conditions has a number of limitations as was pointed out in *Ganushkina et al.* [2014]. At the same time, it is currently the best analytical model that can be used for time-dependent boundary conditions at 10 R_E in the plasma sheet.

Ganushkina et al. [2013, 2014] also discussed the role of the accurate representation of the loss processes for modeled electrons to the atmosphere due to the resonant pitch angle scattering by chorus waves. As was seen from the analysis of model performance, the modeled fluxes for 30–100 keV electrons were higher than that observed at dawn and very close to the observed ones at dusk. This may be due to limitations of the electron lifetimes which were introduced according to *Shprits et al.* [2007] and *Chen et al.* [2005]. Introducing the loss processes due to wave-particle interactions according to recent studies such as by *Orlova and Shprits* [2014] will be part of our future study. *Orlova and Shprits* [2014] presented the lifetimes of 1 keV–2 MeV electrons computed in the Tsyganenko 89 magnetic field model for the night, dawn, prenoon, and postnoon magnetic local time (MLT) sectors for different levels of geomagnetic activity and distances. They developed a realistic chorus lower band and upper band wave models for each MLT sector using the recent statistical studies of CRRES, Polar, and THEMIS observations of wave amplitude, wave normal angle, and wave spectral density distributions as functions of magnetic latitude, distance, and *Kp* index. Separate representations of lifetimes are given for electrons with energies < 10 keV and from 10 keV up to 500 keV. *Shprits et al.* [2007] and *Chen et al.* [2005] representations do not include the energy and MLT dependencies of electron lifetimes. For 100–200 keV electrons, there can be an internal acceleration source due to wave-particle interactions that contributes at this energy. Global simulation results also found that additional acceleration is required [*Varotsou et al.*, 2005; *Horne et al.*, 2006; *Albert et al.*, 2009; *Shprits et al.*, 2009].

Keeping in mind all the efforts of the ongoing work on the improvement of model performance, we presented a working online near-real-time nowcast of low-energy electrons as a very important tool which provides highly valuable output. Low-energy electron fluxes are very important to specify when hazardous satellite surface-charging phenomena are considered. These fluxes constitute the low-energy part of the seed population which is critically important for radiation belt dynamics. IMPTAM output provides a critical link in our ability to understand radiation belt dynamics during magnetic storms.

References

Albert, J. M., N. P Meredith, and R. B. Horne (2009), Three-dimensional diffusion simulation of outer radiation belt electrons during the 9 October 1990 magnetic storm, *J. Geophys. Res.*, *114*, A09214, doi:10.1029/2009JA014336.

Åsnes, A., M. G. G. T. Taylor, A. L. Borg, B. Lavraud, R. W. H. Friedel, C. P. Escoubet, H. Laakso, P. Daly, and A. N. Fazakerley (2008), Multispacecraft observation of electron beam in reconnection region, *J. Geophys. Res.*, *113*, A07S30, doi:10.1029/2007JA012770.

Baker, D. (2001), Satellite anomalies due to space storms, in *Space Storms and Space Weather Hazards*, edited by I. A. Daglis, chap. 10, pp. 251–284, Kluwer, Dordrecht, Netherlands.

Blake, J. B., et al. (2013), The Magnetic Electron Ion Spectrometer (MagEIS) instruments aboard the Radiation Belt Storm Probes (RBSP) spacecraft, *Space Sci. Rev.*, *179*(1–4), 383–421.

Borovsky, J. E., M. F. Thomsen, R. C. Elphic, T. E. Cayton, and D. J. McComas (1998), The transport of plasma sheet material from the distant tail to geosynchronous orbit, *J. Geophys. Res.*, *103*, 20,297–20,331.

Boyle, C., P. Reiff, and M. Hairston (1997), Empirical polar cap potentials, *J. Geophys. Res.*, *102*(A1), 111–125.

Brautigam, D. H., and J. M. Albert (2000), Radial diffusion analysis of outer radiation belt electrons during the October 9, 1990, magnetic storm, *J. Geophys. Res.*, *105*, 291–309.

Burin des Roziers, E., X. Li, D. N. Baker, T. A. Fritz, R. Friedel, T. G. Onsager, and I. Dandouras (2009), Energetic plasma sheet electrons and their relationship with the solar wind: A cluster and geotail study, *J. Geophys. Res.*, *114*, A02220, doi:10.1029/2008JA013696.

Chen, M. W., M. Schulz, P. C. Anderson, G. Lu, G. Germany, and M. Wüest (2005), Storm time distributions of diffuse auroral electron energy and X-ray flux: Comparison of drift-loss simulations with observations, *J. Geophys. Res.*, *110*, A03210, doi:10.1029/2004JA010725.

Chen, M. W., S. Liu, M. Schulz, J. L. Roeder, and L. R. Lyons (2006), Magnetically self-consistent ring current simulations during the 19 October 1998 storm, *J. Geophys. Res.*, *111*, A11S15, doi:10.1029/2006JA011620.

Chen, Y., R. H. W. Friedel, and G. D. Reeves (2006), PSD distributions of energetic electrons in the outer radiation belt during two geospace environment modeling inner magnetosphere/storms selected storms, *J. Geophys. Res.*, *111*, A11S04, doi:10.1029/2006JA011703.

Christon, S. P., D. J. Williams, D. G. Mitchell, L. A. Frank, and C. Y. Huang (1989), Spectral characteristics of plasma sheet ion and electron populations during undisturbed geomagnetic conditions, *J. Geophys. Res.*, *94*(A10), 13,409–13,424, doi:10.1029/JA094iA10p13409.

Christon, S. P., D. J. Williams, D. G. Mitchell, C. Y. Huang, and L. A. Frank (1991), Spectral characteristics of plasma sheet ion and electron populations during disturbed geomagnetic conditions, *J. Geophys. Res.*, *96*, 1–22.

Davis, V. A., M. J. Mandell, and M. F. Thomsen (2008), Representation of the measured geosynchronous plasma environment in spacecraft charging calculations, *J. Geophys. Res.*, *113*, A10204, doi:10.1029/2008JA013116.

Elkington, S. R., M. Wiltberger, A. A. Chan, and D. N. Baker (2004), Physical models of the geospace radiation environment, *J. Atmos. Sol. Terr. Phys.*, *66*, 1371, doi:10.1016/j.jastp.2004.03.023.

Fok, M.-C., et al. (2003), Global ENA IMAGE observations, *Space Sci. Rev.*, *109*, 77–103.

Frezet, M., J. P. Granger, L. Levy, and J. Hamelin (1988), Assessment of charging behaviour of Meteosat spacecraft in geosynchronous environment, ONERA Paper 233-248 presented at CERT, 4th International Conference on Spacecraft Materials in Space Environment, ONERA Toulouse Research Center, Toulouse, France.

Fälthammar, C.-G. (1965), Effects of time-dependent electric fields on geomagnetically trapped radiation, *J. Geophys. Res.*, *70*, 2503–2516.

Funsten, H. O., et al. (2013), Helium, Oxygen, Proton, and Electron (HOPE) mass spectrometer for the radiation belt storm probes mission, *Space Sci. Rev.*, *179*(1–4), 423–484.

Gabrielse, C., V. Angelopoulos, A. Runov, and D. L. Turner (2014), Statistical characteristics of particle injections throughout the equatorial magnetotail, *J. Geophys. Res. Space Physics*, *119*, 2512–2535, doi:10.1002/2013JA019638.

Ganushkina, N. Y., T. I. Pulkkinen, V. F. Bashkirov, D. N. Baker, and X. Li (2001), Formation of intense nose structures, *Geophys. Res. Lett.*, *28*(3), 491–494.

Ganushkina, N. Y., T. I. Pulkkinen, and T. Fritz (2005), Role of substorm-associated impulsive electric fields in the ring current development during storms, *Ann. Geophys.*, *23*, 579–591.

Ganushkina, N. Y., T. I. Pulkkinen, M. Liemohn, and A. Milillo (2006), Evolution of the proton ring current energy distribution during April 21–25, 2001 storm, *J. Geophys. Res.*, *111*, A11S08, doi:10.1029/2006JA011609.

Ganushkina, N. Y. (2011), IMPTAM: Including self-consistent magnetic field in ring current modeling, paper presentation at 2011 Joint CEDARGEM workshop, 26 June–1 July, Santa Fe, N. M.

Ganushkina, N. Y., M. W. Liemohn, and T. I. Pulkkinen (2012a), Storm-time ring current: Model-dependent results, *Ann. Geophys.*, *30*, 177–202.

Ganushkina, N. Y., S. Dubyagin, M. Kubyshkina, M. Liemohn, and A. Runov (2012b), Inner magnetosphere currents during CIR/HSS storm on July 21–23, 2009, *J. Geophys. Res.*, *117*, A00L04, doi:10.1029/2011JA017393.

Ganushkina, N. Y., O. Amariutei, Y. Y. Shpritz, and M. Liemohn (2013), Transport of the plasma sheet electrons to the geostationary distances, *J. Geophys. Res. Space Physics*, *118*, 82–98, doi:10.1002/2012JA017923.

Ganushkina, N. Y., M. Liemohn, O. Amariutei, and D. Pitchford (2014), Low energy electrons (5–50 keV) in the inner magnetosphere, *J. Geophys. Res. Space Physics*, *119*, 246–259, doi:10.1002/2013JA019304.

Garrett, H. B. (1981), The charging of spacecraft surfaces, *Rev. Geophys.*, *19*(4), 577–616, doi:10.1029/RG019i004p00577.

Green, J. C., and M. G. Kivelson (2001), A tale of two theories: How the adiabatic response and ULF waves affect relativistic electrons, *J. Geophys. Res.*, *106*, 25,777–25,791.

Green, J. C., and M. G. Kivelson (2004), Relativistic electrons in the outer radiation belt: Differentiating between acceleration mechanisms, *J. Geophys. Res.*, *109*, A03213, doi:10.1029/2003JA010153.

Hoeber, C. F., E. A. Robertson, I. Katz, V. A. Davis, and D. B. Snyder (1998), Solar array augmented electrostatic discharge in GEO, AIAA Paper 981401 paper presented at 17th AIAA International Communications Spacecraft Systems Conference and Exhibit, Am. Inst. of Aeronaut. and Astron., Yokohama, Japan.

Horne, R. B., and R. M. Thorne (1998), Potential waves for relativistic electron scattering and stochastic acceleration during magnetic storms, *Geophys. Res. Lett.*, *25*, 3011–3014.

Horne, R. B., et al. (2005a), Wave acceleration of electrons in the Van Allen radiation belts, *Nature*, *437*, 227–230, doi:10.1038/nature03939.

Horne, R. B., R. M. Thorne, S. A. Glauert, J. M. Albert, N. P. Meredith, and R. R. Anderson (2005b), Timescale for radiation belt electron acceleration by whistler mode chorus waves, *J. Geophys. Res.*, *110*, A03225, doi:10.1029/2004JA010811.

Horne, R. B., N. P. Meredith, S. A. Glauert, A. Varotsou, R. M. Thorne, Y. Y. Shprits, and R. R. Anderson (2006), Mechanisms for the acceleration of radiation belt electrons, in *Recurrent Magnetic Storms: Corotating Solar Wind Streams, Geophys. Monogr. Ser.*, vol. 167, edited by B. T. Tsurutani et al., pp. 151–173, AGU, Washington, D. C.

Horne, R. B., S. A. Glauert, N. P. Meredith, D. Heynderickx, D. Boscher, V. Maget, and D. Pitchford (2013a), Space Weather effects on satellites and forecasting the Earth's electron radiation belts with SPACECAST, *Space Weather*, *11*, 169–186, doi:10.1002/swe.20023.

Horne, R. B., et al. (2013b), Forecasting the Earth's electrons radiation belts and modeling solar energetic particle events: Recent results from SPACECAST, *J. Space Weather Space Clim.*, *3*, A20, doi:10.1051/swsc/2013042.

Iucci, N., et al. (2005), Space weather conditions and spacecraft anomalies in different orbits, *Space Weather*, *3*, S01001, doi:10.1029/2003SW000056.

Jaggi, R. K., and R. A. Wolf (1973), Self-consistent calculation of the motion of a sheet of ions in the magnetosphere, *J. Geophys. Res.*, *78*, 2852–2866.

Jolliffe, I. T., and D. B. Stephenson (Eds.) (2003), *Forecast Verification: A Practitioner's Guide in Atmospheric Science*, Wiley, Chichester, U. K.

Jordanova, V. K., and Y. S. Miyoshi (2005), Relativistic model of ring current and radiation belt ions and electrons: Initial results, *Geophys. Res. Lett.*, *32*, L14104, doi:10.1029/2005GL023020.

Jordanova, V. K., L. M. Kistler, J. U. Kozyra, G. V. Khazanov, and A. F. Nagy (1996), Collisional losses of ring current ions, *J. Geophys. Res.*, *111–126*(A1), doi:10.1029/95JA02000.

Jordanova, V. K., Y. Yu, J. T. Niehof, R. M. Skoug, G. D. Reeves, C. A. Kletzing, J. F. Fennell, and H. E. Spence (2014), Simulations of inner magnetosphere dynamics with an expanded RAM-SCB model and comparisons with Van Allen Probes observations, *Geophys. Res. Lett.*, *41*, 2687–2694, doi:10.1002/2014GL059533.

Kaufmann, R. L., W. R. Paterson, and L. A. Frank (2005), Relationships between the ion flow speed, magnetic flux transport rate, and other plasma sheet parameters, *J. Geophys. Res.*, *110*, A09216, doi:10.1029/2005JA011068.

Kerns, K. J., D. A. Hardy, and M. S. Gussenhoven (1994), Modeling of convection boundaries seen by CRRES in 120-eV to 28-keV particles, *J. Geophys. Res.*, *99*, 2403–2414.

Khazanov, G. V., M. W. Liemohn, T. S. Newman, M.-C. Fok, and A. J. Ridley (2004), Magnetospheric convection electric field dynamics and stormtime particle energization: Case study of the magnetic storm of 4 May 1998, *Ann. Geophys.*, *22*, 497–510.

Koons, H. C., J. E. Mazur, R. S. Selesnick, J. B. Blake, J. F. Fennell, J. L. Roeder, and P. C. Anderson (1999), The impact of the space environment on space systems, *Aerospace Rep. TR-99 (1670)-1*, Aerospace Corp., El Segundo, Calif.

Lanzerotti, L. J., K. LaFleur, C. G. Maclennan, and D. W. Maurer (1998), Geosynchronous spacecraft charging in January 1997, *Geophys. Res. Lett.*, *25*(15), 2967–2970.

Lejosne, S., D. Boscher, V. Maget, and G. Rolland (2013), Deriving electromagnetic radial diffusion coefficients of radiation belt equatorial particles for different levels of magnetic activity based on magnetic field measurements at geostationary orbit, *J. Geophys. Res. Space Physics*, *118*, 3147–3156, doi:10.1002/jgra.50361.

Liemohn, M. W., and P. C. Brandt (2005), Small-scale structure in the stormtime ring current, in *Inner Magnetosphere Interactions: New Perspectives From Imaging, Geophys. Monogr. Ser.*, vol. 159, edited by J. L. Burch, M. Schulz, and H. Spence, p. 167, AGU, Washington, D. C.

Liemohn, M. W., G. V. Khazanov, and J. U. Kozyra (1998), Banded electron structure formation in the inner magnetosphere, *Geophys. Res. Lett.*, *25*, 877–880.

Mauk, B. H., and C.-I. Meng (1983), Characterization of geostationary particle signatures based on the "Injection Boundary" model, *J. Geophys. Res.*, *88*, 3055–3071.

Miyoshi, Y. S., V. K. Jordanova, A. Morioka, M. F. Thomsen, G. D. Reeves, D. S. Evans, and J. C. Green (2006), Observations and modeling of energetic electron dynamics during the October 2001 storm, *J. Geophys. Res.*, *111*, A11S02, doi:10.1029/2005JA011351.

National Research Council Report (2008), Severe space weather events understanding societal and economic impacts, Washington D. C. USA. [Available at www.nap.edu].

Orlova, K., and Y. Shprits (2014), Model of lifetimes of the outer radiation belt electrons in a realistic magnetic field using realistic chorus wave parameters, *J. Geophys. Res. Space Physics*, *119*, 770–780, doi:10.1002/2013JA019596.

O'Brien, T. P. (2009), SEAES-GEO: A spacecraft environmental anomalies expert system for geosynchronous orbit, *Space Weather*, *7*, S09003, doi:10.1029/2009SW000473.

Purvis, C. K., H. B. Garrett, A. C. Whittlesey, and N. J. Stevens (1984), Design guidelines for assessing and controlling spacecraft charging effects, *NASA Tech. Rep. NASA-TR 2361*, Lewis Research Center, Cleveland, Ohio.

Reeves, G. D., K. L. McAdams, R. H. W. Friedel, and T. P. O'Brien (2003), Acceleration and loss of relativistic electrons during geomagnetic storms, *Geophys. Res. Lett.*, *30*(10), 1529, doi:10.1029/2002GL016513.

Ridley, A. J., and M. W. Liemohn (2002), A model-derived description of the penetration electric field, *J. Geophys. Res.*, *107*(A8), 1151, doi:10.1029/2001JA000051.

Roederer, J. G. (1970), *Dynamics of Geomagnetically Trapped Radiation*, p. 36, Springer, New York.

Schulz, M., and L. Lanzerotti (1974), *Particle Diffusion in the Radiation Belts*, Springer, New York.

Shprits, Y. Y., and R. M. Thorne (2004), Time dependent radial diffusion modeling of relativistic electrons with realistic loss rates, *Geophys. Res. Lett.*, *31*, L08805, doi:10.1029/2004GL019591.

Shprits, Y. Y., R. M. Thorne, G. D. Reeves, and R. Friedel (2005), Radial diffusion modeling with empirical lifetimes: Comparison with CRRES observations, *Ann. Geophys.*, *23*, 1467–1471.

Shprits, Y. Y., R. M. Thorne, R. B. Horne, and D. Summers (2006), Bounce-averaged diffusion coefficients for field-aligned chorus waves, *J. Geophys. Res.*, *111*, A10225, doi:10.1029/2006JA011725.

Shprits, Y. Y., N. P. Meredith, and R. M. Thorne (2007), Parameterization of radiation belt electron loss timescales due to interactions with chorus waves, *Geophys. Res. Lett.*, *34*, L11110, doi:10.1029/2006GL029050.

Shprits, Y. Y., D. Subbotin, and B. Ni (2009), Evolution of electron fluxes in the outer radiation belt computed with the VERB code, *J. Geophys. Res.*, *114*, A11209, doi:10.1029/2008JA013784.

Spence, H. E., et al. (2013), Science goals and overview of the Radiation Belt Storm Probes (RBSP) Energetic Particle, Composition, and Thermal Plasma (ECT) suite on NASA's Van Allen Probes mission, *Space Sci. Rev.*, *179*(1–4), 311–336.

Subbotin, D. A., and Y. Y. Shprits (2009), Three-dimensional modeling of the radiation belts using the Versatile 24 Electron Radiation Belt (VERB) code, *Space Weather*, *7*, S10001, doi:10.1029/2008SW000452.

Summers, D., R. M. Thorne, and F. Xiao (1998), Relativistic theory of wave-particle resonant diffusion with application to electron acceleration in the magnetosphere, *J. Geophys. Res.*, *103*, 20,487–20,500.

Tsyganenko, N. A. (1995), Modeling the Earth's magnetospheric magnetic field confined within a realistic magnetopause, *J. Geophys. Res.*, *100*, 5599–5612.

Tsyganenko, N. A., and T. Mukai (2003), Tail plasma sheet models derived from Geotail particle data, *J. Geophys. Res.*, *108*(A3), 1136, doi:10.1029/2002JA009707.

Varotsou, A., D. Boscher, S. Bourdarie, R. B. Horne, S. A. Glauert, and N. P. Meredith (2005), Simulation of the outer radiation belt electrons near geosynchronous orbit including both radial diffusion and resonant interaction with whistler-mode chorus waves, *Geophys. Res. Lett.*, *32*, L19106, doi:10.1029/2005GL023.

Vasyliunas, V. M. (1968), A survey of low-energy electrons in the evening sector of the magnetosphere with OGO 1 and OGO 3, *J. Geophys. Res.*, *73*, 2839–2852, doi:10.1029/JA073i009p02839.

Walsh, A. P., A. N. Fazakerley, C. Forsyth, C. J. Owen, M. G. G. T. Taylor, and I. J. Rae (2013), Sources of electron pitch angle anisotropy in the magnetotail plasma sheet, *J. Geophys. Res. Space Physics*, *118*, 6042–6054, doi:10.1002/jgra.50553.

Wang, C.-P., M. Gkioulidou, L. R. Lyons, and V. Angelopoulos (2012), Spatial distributions of the ion to electron temperature ratio in the magnetosheath and plasma sheet, *J. Geophys. Res.*, *117*, A08215, doi:10.1029/2012JA017658.

Whipple, E. C. (1981), Potentials of surfaces in space, *Rep. Prog. Phys.*, *44*, 1197, doi:10.1088/0034-4885/44/11/002.

Wrenn, G. L. (1995), Conclusive evidence for internal dielectric charging anomalies on geosynchronous communications spacecraft, *J. Spacecraft Rockets*, *32*, 514.